# Detection of the [O i] 63 μm emission line from the z = 6.04 quasar J2054-0005

Ishii, Nozomi; Hashimoto, Takuya; Ferkinhoff, Carl; Rybak, Matus; Inoue, Akio K.; Michiyama, Tomonari; Donevski, Darko; Fujimoto, Seiji; More Authors; Salak, Dragan

**DOI**
10.1093/pasj/psae105

**Publication date**
2025

**Document Version**
Final published version

**Published in**
Publications of the Astronomical Society of Japan

*Publications of the Astronomical Society of Japan*, 2025, **77**(1), 139–148
https://doi.org/10.1093/pasj/psae105
Advance access publication date: 2024 December 26

# Detection of the [O I] 63 μm emission line from the $z = 6.04$ quasar J2054–0005

**Nozomi Ishii,[1,2] Takuya Hashimoto,[1,3,*] Carl Ferkinhoff,[4] Matus Rybak,[5,6,7] Akio K. Inoue,[8,9] Tomonari Michiyama,[10] Darko Donevski,[11,12] Seiji Fujimoto,[13] Dragan Salak,[14,15] Nario Kuno,[1,3] Hiroshi Matsuo,[16,17] Ken Mawatari,[1,3,9] Yoichi Tamura,[18] Takuma Izumi,[16,17] Tohru Nagao,[19] Yurina Nakazato,[20] Wataru Osone,[1] Yuma Sugahara,[9,15] Mitsutaka Usui,[1] Koki Wakasugi,[1] Hidenobu Yajima,[1,21] Tom J. L. C. Bakx,[22] Yoshinobu Fudamoto,[23] Romain A. Meyer,[24] Fabian Walter,[25] and Naoki Yoshida[20,26,27]**

[1] Graduate School of Pure and Applied Sciences, University of Tsukuba, 1-1-1 Tennodai, Tsukuba, Ibaraki 305-8571, Japan
[2] Systems Engineering Consultants Co., Ltd (SEC), Setagaya Business Square 4-10-1 Yoga, Setagaya-ku, Tokyo 158-0097, Japan
[3] Tomonaga Center for the History of the Universe, University of Tsukuba, 1-1-1 Tennodai, Tsukuba, Ibaraki 305-8571, Japan
[4] Department of Physics, Winona State University, 175 West Mark Street, Winona, MN 55987, USA
[5] Faculty of Electrical Engineering, Mathematics and Computer Science, Delft University of Technology, Mekelweg 4, 2628 CD Delft, The Netherlands
[6] Leiden Observatory, Leiden University, PO Box 9513, 2300 RA Leiden, The Netherlands
[7] SRON–Netherlands Institute for Space Research, Niels Bohrweg 4, 2333 CA Leiden, The Netherlands
[8] Department of Physics, School of Advanced Science and Engineering, Faculty of Science and Engineering, Waseda University, 3-4-1 Okubo, Shinjuku, Tokyo 169-8555, Japan
[9] Waseda Research Institute for Science and Engineering, Faculty of Science and Engineering, Waseda University, 3-4-1 Okubo, Shinjuku, Tokyo 169-8555, Japan
[10] Faculty of Information Science, Shunan University, 843-4-2 Gakuendai, Shunanshi, Yamaguchi 745-8566, Japan
[11] National Center for Nuclear Research, Pasteura 7, 02-093 Warsaw, Poland
[12] SISSA-Scuola Internazionale Superiore di Studi Avanzati, Via Bonomea 265, 34136 Trieste, Italy
[13] Department of Astronomy, The University of Texas at Austin, 2515 Speedway, Stop C1400, Austin, TX 78712, USA
[14] Institute for the Advancement of Higher Education, Hokkaido University, Kita 17 Nishi 8, Kita-ku, Sapporo, Hokkaido 060-0817, Japan
[15] Department of Cosmosciences, Graduate School of Science, Hokkaido University, Kita 10 Nishi 8, Kita-ku, Sapporo, Hokkaido 060-0810, Japan
[16] National Astronomical Observatory of Japan, 2-21-1 Osawa, Mitaka, Tokyo 181-8588, Japan
[17] The Graduate University for Advanced Studies (SOKENDAI), 2-21-1 Osawa, Mitaka, Tokyo 181-8588, Japan
[18] Department of Physics, Graduate School of Science, Nagoya University Furo, Chikusa, Nagoya, Aichi 464-8602, Japan
[19] Research Center for Space and Cosmic Evolution, Ehime University, 2-5 Bunkyo-cho, Matsuyama, Ehime 790-8577, Japan
[20] Department of Physics, The University of Tokyo, 7-3-1 Hongo, Bunkyo, Tokyo 113-0033, Japan
[21] Center for Computational Sciences, University of Tsukuba, 1-1-1 Tennodai, Tsukuba, Ibaraki 305-8577, Japan
[22] Department of Earth and Space Sciences, Chalmers University of Technology, Onsala Observatory, SE-439 90 Onsala, Sweden
[23] Center for Frontier Science, Chiba University, 1-33 Yayoi-cho, Inage-ku, Chiba 263-8522, Japan
[24] Department of Astronomy, University of Geneva, Chemin Pegasi 51, CH-1290 Versoix, Switzerland
[25] Max-Planck-Institut für Astronomie, Königstuhl 17, D-69117 Heidelberg, Germany
[26] Kavli Institute for the Physics and Mathematics of the Universe (WPI), UT Institute for Advanced Study, The University of Tokyo, 5-1-5 Kashiwanoha, Kashiwa, Chiba 277-8583, Japan
[27] Research Center for the Early Universe, School of Science, The University of Tokyo, 7-3-1 Hongo, Bunkyo, Tokyo 113-0033, Japan

*E-mails: hashimoto.takuya.ga@u.tsukuba.ac.jp; thashimoto@est.osaka-sandai.ac.jp

## Abstract

We report the highest-redshift detection of [O I] 63 μm from a luminous quasar, J2054−0005, at $z = 6.04$ based on the Atacama Large Millimeter/sub-millimeter Array (ALMA) Band 9 observations. The [O I] 63 μm line luminosity is $(4.5 \pm 1.5) \times 10^9 L_\odot$, corresponding to the [O I] 63 μm-to-far-infrared luminosity ratio of $\approx 6.7 \times 10^{-4}$, which is consistent with the value obtained in the local Universe. Remarkably, [O I] 63 μm is as bright as [C II] 158 μm, resulting in the [O I]-to-[C II] line luminosity ratio of $1.3 \pm 0.5$. Based on a careful comparison of the luminosity ratios of [O I] 63 μm, [C II] 158 μm, and dust continuum emission to models of photodissociation regions, we find that J2054−0005 has a gas density $\log(n_{\rm H}/{\rm cm}^{-3}) = 3.7 \pm 0.3$ and an incident far-ultraviolet radiation field of $\log(G/G_0) = 3.0 \pm 0.1$, showing that [O I] 63 μm serves as an important coolant of the dense and warm gas in J2054−0005. A close examination of the [O I] and [C II] line profiles suggests that the [O I] line may be partially self-absorbed; however, deeper observations are needed to verify this conclusion. Regardless, the gas density and incident radiation field are in broad agreement with the values obtained in nearby star-forming galaxies and objects with [O I] 63 μm observations at $z = 1$–3 with

**Received:** 2024 August 20; **Accepted:** 2024 November 26

the Herschel Space Observatory. These results demonstrate the power of ALMA high-frequency observations targeting [O I] 63 μm to examine the properties of photodissociation regions in high-redshift galaxies.

**Keywords:** galaxies: active — galaxies: high-redshift — galaxies: ISM — quasars: general

## 1 Introduction

Quasars are powered by supermassive black holes (SMBHs) with masses of $\sim 10^{8-10}\,M_\odot$ (e.g., Inayoshi et al. 2020 and references therein). In the local Universe, there is a well known correlation between the central black hole mass and the bulge mass (e.g., Kormendy & Ho 2013). Given the coevolution of SMBHs and their host galaxies, understanding detailed properties of the host galaxies in the early Universe is key to understanding the formation and evolution of SMBHs (e.g., Valiante et al. 2017).

The interstellar medium (ISM) of high-redshift ($z$) quasar host galaxies is often studied with the brightest far-infrared (FIR) fine-structure line, [C II] 158 μm, as well as with carbon monoxide (CO) emission lines and dust continuum emission (e.g., Venemans et al. 2018; Decarli et al. 2018, 2022; Izumi et al. 2019; Pensabene et al. 2024; Tripodi et al. 2024). These studies have shown that the quasar host galaxies can be characterized by high star-formation rates (SFR $\sim$ 50–3000 $M_\odot$ yr$^{-1}$), molecular gas masses ($\sim 10^{10}\,M_\odot$), and dust masses ($\sim 10^{7-9}\,M_\odot$).

The [O I] $^3P_2 \rightarrow {}^3P_1$ line at the rest-frame wavelength of 63 μm (rest-frame frequency of 4744.77749 GHz), hereafter [O I] 63 μm, has a critical density of $n_{\rm H,crit.} \sim 2.5 \times 10^5$ cm$^{-3}$ at the temperature of 100 K and emitting level with an equivalent temperature of $T_* = \Delta E/k = 228$ K above the ground (Draine 2011). Compared to the critical density of [C II] 158 μm, $n_{\rm H,crit.} \sim 3 \times 10^3$ cm$^{-3}$ at the temperature of 100 K, and the equivalent temperature $T_* = \Delta E/k = 91.25$ K, the [O I] 63 μm line traces high-density, high-temperature neutral gas (Kaufman et al. 1999, 2006; Narayanan & Krumholz 2017). Thus, combinations of [O I] 63 μm, [C II] 158 μm, and dust continuum data allow us to estimate the gas density and temperature in photodissociated regions (PDRs). Due to the high equivalent temperature, [O I] 63 μm also has an advantage that it is less affected by the cosmic microwave background radiation, which makes it a reliable tracer of neutral ISM at high redshift.

Initial campaigns for the [O I] 63 μm line observations include the NASA Learjet telescope system targeting the Orion nebula (M42) and Omega nebula (M17) (Melnick et al. 1979) and a balloon-borne telescope targeting the Orion nebula (Furniss et al. 1983). The [O I] 63 μm line was observed in external galaxies with the Infrared Space Observatory (ISO) (e.g., Malhotra et al. 2001; Brauher et al. 2008) and the Herschel Space Observatory (hereafter Herschel) (e.g., Farrah et al. 2013; Madden et al. 2013; Cormier et al. 2015; Diaz-Santos et al. 2017; Herrera-Camus et al. 2018) in metal-rich spiral galaxies, ultra-luminous infrared galaxies (ULIRGs), and blue compact dwarf galaxies. These observations showed that [O I] 63 μm is a dominant coolant in dense PDRs, with a typical [O I]-to-FIR luminosity ratio $L_{[\rm O\,I]63\,\mu m}/L_{\rm FIR} \approx 10^{-4}$–$10^{-3}$, where $L_{\rm FIR}$ is integrated over 42–122 μm.

The [O I] 63 μm line observations at $z \sim$ 1–3 were conducted by Herschel, mainly in gravitationally lensed submillimeter galaxies (SMGs) (e.g., Sturm et al. 2010; Coppin et al. 2012; Brisbin et al. 2015; Wardlow et al. 2017; Zhang et al. 2018; Wagg et al. 2020) and in the Cloverleaf quasar at $z = 2.46$ (Uzgil et al. 2016). The detections revealed enhanced luminosity ratios, $L_{[\rm O\,I]63\,\mu m}/L_{\rm FIR}$ ranging from $\approx 10^{-3}$ to $10^{-2}$, but still with a limited number of detections ($N \sim 15$). On the other hand, stacking of the non-detections of individual SMGs in Wardlow et al. (2017) resulted in a detection of [O I] 63 μm, yielding $L_{[\rm O\,I]63\,\mu m}/L_{\rm FIR} = (3.6 \pm 1.2) \times 10^{-4}$, showing a diversity in the ISM properties of high-$z$ galaxies.

At $z \sim$ 4–7, the [O I] 63 μm line can be observed from the ground with, e.g., the Atacama Large Millimeter/submillimeter Array (ALMA) in Bands 9–10. The [O I] 63 μm line observation at $z > 4$ was first reported by Rybak et al. (2020). The authors observed a gravitationally lensed SMG, G09 83808, at $z = 6.027$ with the Atacama Pathfinder EXperiment (APEX) 12 m telescope. Although a $5\sigma$ [O I] 63 μm line was initially reported, subsequent follow-up observations with ALMA Band 9 did not confirm the line (Rybak et al. 2023). Litke et al. (2022) targeted [O I] 63 μm along with other FIR lines in a gravitationally lensed SMG, SPT 0346-52, at $z = 5.656$ with ALMA Band 9, resulting in a non-detection of [O I] 63 μm. The first detection of [O I] 63 μm at $z > 4$ was recently made with ALMA Band 10 in a non-lensed hyper-luminous ($L_{\rm FIR} \sim 3.5 \times 10^{13} L_\odot$) active galactic nucleus (AGN), W2246−0526, at $z = 4.6$ (Fernández Aranda et al. 2024). Clearly, the number of [O I] 63 μm observations at $z > 4$ is still scarce. A contributing factor to this scarcity may be that [O I] 63 μm emission is typically optically thick (e.g., Goldsmith et al. 2021), unlike most far-IR fine-structure lines like [C II] 158 μm. As such, [O I] 63 μm emission is detected only from front faces of emitting clouds. Additionally, if sufficient neutral oxygen is along the line of sight in a galaxy, the [O I] 63 μm line can be readily self-absorbed. For example, self-absorption is seen in a nearby large molecular cloud DR 21 (Poglitsch et al. 1996), a diffused nebula NGC 6334 (Kraemer et al. 1998), and a highly obscured H II region Sgr B2 (Baluteau et al. 1997) with massive star-formation activity. In extra-galactic sources, nearly half of the local ULIRGS in Rosenberg et al. (2015) show significant missing flux with several sources showing the 63 μm line nearly completely absorbed (see also González-Alfonso et al. 2012). Determining whether [O I] 63 μm emission is optically thick requires comparing the line to the optically thin [O I] 145 μm line, while assessing self-absorption requires a significant signal-to-noise ratio in the spectrum to identify absorption features. Fernández Aranda et al. (2024) detect both the [O I] 63 and 145 μm lines, and their line ratios suggest that the [O I] 63 μm line emission is indeed optically thick. However, the data were not sensitive enough to identify the narrow absorption feature in W2246−0526.

In this paper, we report a new detection of [O I] 63 μm in a distant quasar, SDSS J2054−0005, at $z = 6.0$ based on ALMA Band 9 archival data (section 2). To date, this is the most distant detection of [O I] 63 μm. We present our calculations on

**Table 1.** ALMA Band 9 data.

| Data | Achieved sensitivity in rms | Beam size FWHM | Beam PA |
|---|---|---|---|
| Dust continuum | 0.55 mJy beam$^{-1}$ | $0\farcs64 \times 0\farcs56$ | 72° |
| [O I] 63 μm cube (50 km s$^{-1}$ bin) | 3.68 mJy beam$^{-1}$ | $0\farcs65 \times 0\farcs56$ | 83° |

the [O I] 63 μm luminosity and its luminosity ratios against $L_{\rm FIR}$ and the [C II] 158 μm luminosity in section 3. In section 4, we perform PDR modeling to constrain the neutral gas properties. We summarize our results in section 5.

Throughout this paper, we assume a Λ cold dark matter cosmology with $\Omega_m = 0.272$, $\Omega_\Lambda = 0.728$, and $H_0 = 70.4$ km s$^{-1}$ Mpc$^{-1}$ (Komatsu et al. 2011). At the redshift of the source ($z = 6.04$), the age of the Universe is 0.946 Gyr and an angular size of 1″ corresponds to a proper distance of 5.85 kpc. The solar luminosity is $L_\odot = 3.839 \times 10^{33}$ erg s$^{-1}$.

## 2 Observations and data

### 2.1 The target: J2054−0005

The quasar J2054−0005 was originally discovered in the Sloan Digital Sky Survey (SDSS) (Jiang et al. 2008), and later detected in various emission lines of [C II] 158 μm (e.g., Wang et al. 2013; Venemans et al. 2020), [O III] 88 μm (Hashimoto et al. 2019), CO(2–1) and CO(6–5) (Shao et al. 2019), and CO(7–6) (Decarli et al. 2022), as well as in the OH 119 μm absorption and emission (Salak et al. 2024). The redshift determined from these lines is $6.0391 \pm 0.0002$. J2054−0005 was also observed in [C I](2–1); however, it resulted in a non-detection (Decarli et al. 2022).

J2054−0005 is a non-lensed quasar, and has a bolometric luminosity of $\approx 3 \times 10^{13} L_\odot$ (Wang et al. 2013; Farina et al. 2022). The black hole mass is estimated to be $\sim$(1.5–10.2) $\times 10^9 M_\odot$ based on the single-epoch technique with an Eddington ratio of $\lambda_{\rm Edd} \sim 0.1$–0.7 (Farina et al. 2022). Based on a fit to multi-wavelength dust continuum data, J2054−0005 has a total infrared luminosity integrated over 8–1000 μm, $L_{\rm TIR}$, $\approx 1 \times 10^{13} L_\odot$ (Wang et al. 2013; Hashimoto et al. 2019; Tripodi et al. 2024), making it one of the brightest quasars at $z \gtrsim 6$. The SFR estimated from $L_{\rm TIR}$ is $\approx 800\, M_\odot$ yr$^{-1}$ after a correction of the AGN contribution (Salak et al. 2024).

### 2.2 ALMA Band 9 data

ALMA Band 9 observation was carried out on 2017 March 22 as part of the ALMA Cycle 4 program (Project ID: 2016.1.01063.S, PI: C. Ferkinhoff). The antennas of the 12 m array observed a single field centered at ($\alpha_{\rm ICRS}$, $\delta_{\rm ICRS}$) = ($20^{\rm h}54^{\rm m}06\fs490$, $-00°05'14\farcs80$). 42 antennas were used, with baseline lengths ranging from 15.1–278.9 m. This resulted in a maximum recoverable scale of 4″.2 and a field of view of 8″.6. The on-source integration time was 39 min.

Four spectral windows were set at central frequencies of 672.3, 674.1, 676.0, and 677.8 GHz, referred to as SPW1, SPW2, SPW3, and SPW4, respectively. SPW2 observed the [O I] 63 μm line, whereas the other three SPWs observed dust continuum emission. The quasars J1924−2914 and J2025−0735 were used for the bandpass and complex gain calibration, respectively. The flux was scaled using Titan, yielding a calibration uncertainty of less than 20% in ALMA Band 9, according to the ALMA Cycle 4 Proposer's Guide.[1]

The data were reduced with the Common Astronomy Software Applications (CASA; CASA Team 2022) version 4.7.0. The CASA `tclean` task was used for imaging, with a natural weighting to optimize the point-source sensitivity. Table 1 summarizes the resulting resolution and sensitivity of the data.

Continuum maps were created using all channels except for SPW2 that included [O I] 63 μm. The synthesized beam has a size of $0\farcs64 \times 0\farcs56$ in the FWHM and a positional angle of 72°. The rms of the map is 0.55mJy beam$^{-1}$.

To create line cubes in SPW2, the CASA task `imcontsub`[2] was first applied to subtract the continuum emission. We then created cubes with a velocity width of 50 km s$^{-1}$ without *uv*-tapering. The cube has a synthesized beam size of $0\farcs65 \times 0\farcs56$ and a positional angle of 83°. The typical rms sensitivity of the cube is 3.68 mJy beam$^{-1}$ per 50 km s$^{-1}$ bin.

## 3 Results

### 3.1 63 μm continuum emission

The data probe the dust continuum emission at a rest-frame wavelength of $\lambda_{\rm rest} \approx 63$ μm. The dust continuum emission is detected at a peak significance of 13$\sigma$, as shown in the left panel of figure 1. With the CASA task `imfit`, we obtain the flux density of $S_{\nu,63\,\mu{\rm m}} = 9.6 \pm 1.0$ mJy (table 2). The peak position is at ($\alpha_{\rm ICRS}$, $\delta_{\rm ICRS}$) = ($20^{\rm h}54^{\rm m}06\fs495$, $-00°05'14\farcs46$), well consistent with previous dust continuum positions (e.g., Wang et al. 2013; Hashimoto et al. 2019; Salak et al. 2024). The beam-deconvolved size of the continuum-emitting region is ($0\farcs42 \pm 0\farcs13$) × ($0\farcs23 \pm 0\farcs09$), consistent with previous measurements within 2$\sigma$ uncertainties: ($0\farcs23 \pm 0\farcs01$) × ($0\farcs15 \pm 0\farcs02$) at $\lambda_{\rm rest} \approx 87$ μm (Hashimoto et al. 2019) and ($0\farcs27 \pm 0\farcs03$) × ($0\farcs26 \pm 0\farcs03$) at $\lambda_{\rm rest} \approx 160$ μm (Wang et al. 2013). Finally, we note that results for the ALMA Band 9 dust continuum have been recently reported in Tripodi et al. (2024) based on the same data set. Our results are consistent with their results in the size and flux density measurements. Hereafter, we focus on [O I] 63 μm in this study.

### 3.2 [O I] 63 μm

The middle panel of figure 1 shows the [O I] 63 μm intensity map (i.e., moment 0 map) integrated over the frequency range of 673.96–674.44 GHz, corresponding to a velocity width of 250 km s$^{-1}$ (≈FWHMs of [C II] 158 μm and [O III] 88 μm) centered at the observed redshift of 6.0391. The noise level of

[1] ⟨https://almascience.nao.ac.jp/proposing/documents-and-tools/cycle4/alma-proposers-guide⟩.

[2] The phase-tracking center of the ALMA Band 9 observation is slightly offset from the position of J2054−0005, ($\alpha_{\rm ICRS}$, $\delta_{\rm ICRS}$) = ($20^{\rm h}54^{\rm m}06\fs503$, $-00°05'14\farcs43$) in Hashimoto et al. (2019). In this case, `imcontsub` optimally subtracts the continuum compared with the CASA task `uvcontsub` (see, e.g., Kaasinen et al. 2023 for the choice of `imcontsub` due to the same issue).

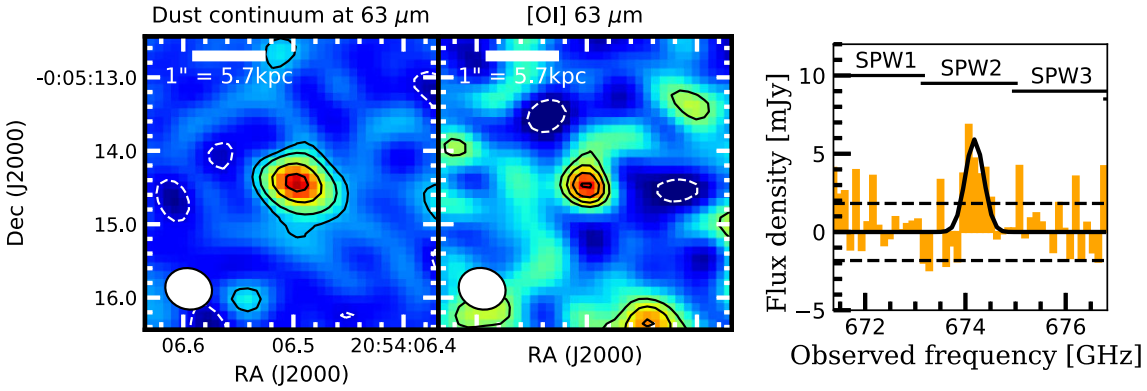


**Fig. 1** Dust continuum map at ≈ 63 μm (left), [O I] 63 μm integrated intensity map (middle), and continuum-subtracted [O I] 63 μm spectrum (right). In the left and middle panels, the ellipse at the lower left corner indicates the synthesized beam size of ALMA. The dust continuum contours are drawn at $\pm(2, 4, 8, 12) \times \sigma$, where $\sigma = 0.55$ mJy beam$^{-1}$. The [O I] 63 μm line contours are drawn at $\pm(2, 3, 4, 5) \times \sigma$, where $\sigma = 0.42$ Jy beam$^{-1}$ km s$^{-1}$. Negative and positive contours are shown by the white dashed and black solid lines, respectively. In the right panel, the continuum-subtracted [O I] 63 μm spectrum is extracted from the region with >2$\sigma$ detection in the integrated intensity map. The black solid line is the best-fitting Gaussian for the line, whereas the black dashed lines show the typical $\pm1\sigma$ noise level measured from the spectrum. The upper horizontal bars indicate the frequency coverages of SPWs 1–3.

**Table 2.** Summary of observational results.

| | [O I] 63 μm |
|---|---|
| $z$ | $6.0385 \pm 0.0005$ |
| FWHM (km s$^{-1}$) | $192 \pm 49$ |
| $S_{[\mathrm{O\,I}]63}\Delta v$ (Jy km s$^{-1}$) | $1.81 \pm 0.61$ |
| $L_{[\mathrm{O\,I}]63}$ ($L_\odot$) | $(4.5 \pm 1.5) \times 10^9$ |
| Size (beam-convolved) | $(0\farcs58 \pm 0\farcs11) \times (0\farcs51 \pm 0\farcs08)$ |
| Size (beam-deconvolved) | $< (0\farcs42 \times 0\farcs23)$ |
| | Dust continuum |
| $S_{\nu,63\,\mu\mathrm{m}}$ (mJy) | $9.6 \pm 1.0$ |
| Size (beam-convolved) | $(0\farcs76 \pm 0\farcs02) \times (0\farcs61 \pm 0\farcs02)$ |
| Size (beam-deconvolved) | $(0\farcs42 \pm 0\farcs13) \times (0\farcs23 \pm 0\farcs09)$ |

the map is $\sigma = 0.42$ Jy beam$^{-1}$ km s$^{-1}$. The line is detected at the peak significance level of $5.0\sigma$. The peak position is at $(\alpha_{\mathrm{ICRS}}, \delta_{\mathrm{ICRS}}) = (20^{\mathrm{h}}54^{\mathrm{m}}06\farcs501, -00^\circ05'14\farcs42)$, well consistent with those for other emission lines (see Salak et al. 2024 for a detailed comparison on the peak positions of emission lines and the optical continuum emission from the quasar).

The right panel of figure 1 shows the continuum-subtracted spectrum extracted from an aperture that encloses the $2\sigma$ region in the integrated intensity map. We apply a Gaussian profile to the spectrum with the *SciPy* `curve_fit` function, where we use the SPWs of 1, 2, and 3. To obtain uncertainties on fitting parameters, the noise level is measured from the frequency ranges in [671.3:673.5] GHz and [674.6:676.8] GHz. We obtain the line FWHM of $192 \pm 49$ km s$^{-1}$ and $z = 6.0385 \pm 0.0005$. We measure the line flux with the CASA task `imfit` assuming a 2D Gaussian profile for the intensity map integrated over a velocity width of 500 km s$^{-1}$ (≈2.6 × FWHM), resulting in $1.81 \pm 0.61$ Jy km s$^{-1}$. With equation (1) (Solomon et al. 1992), the luminosity is estimated to be $(4.53 \pm 1.52) \times 10^9 L_\odot$,

$$L_{\mathrm{line}} = 1.04 \times 10^{-3} \left(\frac{S_{\mathrm{line}}\Delta v}{\mathrm{Jy\,km\,s^{-1}}}\right) \left(\frac{D_{\mathrm{L}}}{\mathrm{Mpc}}\right)^2 \left(\frac{\nu_{\mathrm{obs}}}{\mathrm{GHz}}\right) L_\odot, \quad (1)$$

where $S_{\mathrm{line}}\Delta v$, $D_{\mathrm{L}}$, and $\nu_{\mathrm{obs}}$ are the line flux, luminosity distance, and observed frequency, respectively. The [O I] 63 μm-emitting region is not spatially resolved. Under a reasonable assumption that the region has a smaller size than the continuum-emitting region (figure 1), we obtain the upper limit on the size to be $0\farcs42 \times 0\farcs23$. Table 2 summarizes the observational results.

**Table 3.** Summary of the luminosities in J2054−0005.

| Lines | FWHM (km s$^{-1}$) | Luminosity ($L_\odot$) | Reference |
|---|---|---|---|
| [O I] 63 μm | $192 \pm 49$ | $(4.5 \pm 1.5) \times 10^9$ | This study |
| [C II] 158 μm | $243 \pm 10$ | $(3.4 \pm 0.5) \times 10^9$ | Wang et al. (2013) |
| [O III] 88 μm | $282 \pm 17$ | $(6.8 \pm 0.6) \times 10^9$ | Hashimoto et al. (2019) |
| [C I](2–1) | — | $<1.1 \times 10^8$ | Decarli et al. (2022) |
| FIR | — | $(6.8 \pm 0.2) \times 10^{12}$ | Salak et al. (2024) |

## 3.3 Luminosity ratios

Table 3 summarizes the previous line observations for J2054−0005.[3] We also list $L_{\mathrm{FIR}}$ obtained by Salak et al. (2024) who have performed multi-wavelength spectral energy distribution (SED) fitting for J2054−0005 using `CIGALE` (Boquien et al. 2019) that includes the contribution from both star-formation and AGN activity. We obtain $L_{[\mathrm{O\,I}]63\,\mu\mathrm{m}}/L_{\mathrm{FIR}} = (6.7 \pm 2.2) \times 10^{-4}$ and $L_{[\mathrm{O\,I}]63\,\mu\mathrm{m}}/L_{[\mathrm{C\,II}]158\,\mu\mathrm{m}} = 1.3 \pm 0.5$.

### 3.3.1 $L_{\mathrm{FIR}}$ vs. $L_{[\mathrm{O\,I}]63\,\mu\mathrm{m}}/L_{\mathrm{FIR}}$

The left panel of figure 2 shows a comparison of $L_{[\mathrm{O\,I}]63\,\mu\mathrm{m}}/L_{\mathrm{FIR}}$ with the literature values. These include nearby (U)LIRGs in the GOALS survey (Diaz-Santos et al. 2017; small gray circles), blue compact dwarf galaxies in the Herschel Dwarf Galaxy survey (Cormier et al. 2015; small blue circles), and a compilation of other local galaxies observed by ISO (Coppin et al. 2012; small black circles[4]). De Looze et al. (2014) have obtained an empirical relation between SFR and $L_{[\mathrm{O\,I}]63\,\mu\mathrm{m}}$ in the local Universe. The

[3] The line luminosities of [C II] 158 μm (Wang et al. 2013) and [O III] 88 μm (Hashimoto et al. 2019) are obtained in the same manner as in [O I] 63 μm.

[4] We have removed objects overlapping with those from Diaz-Santos et al. (2017).

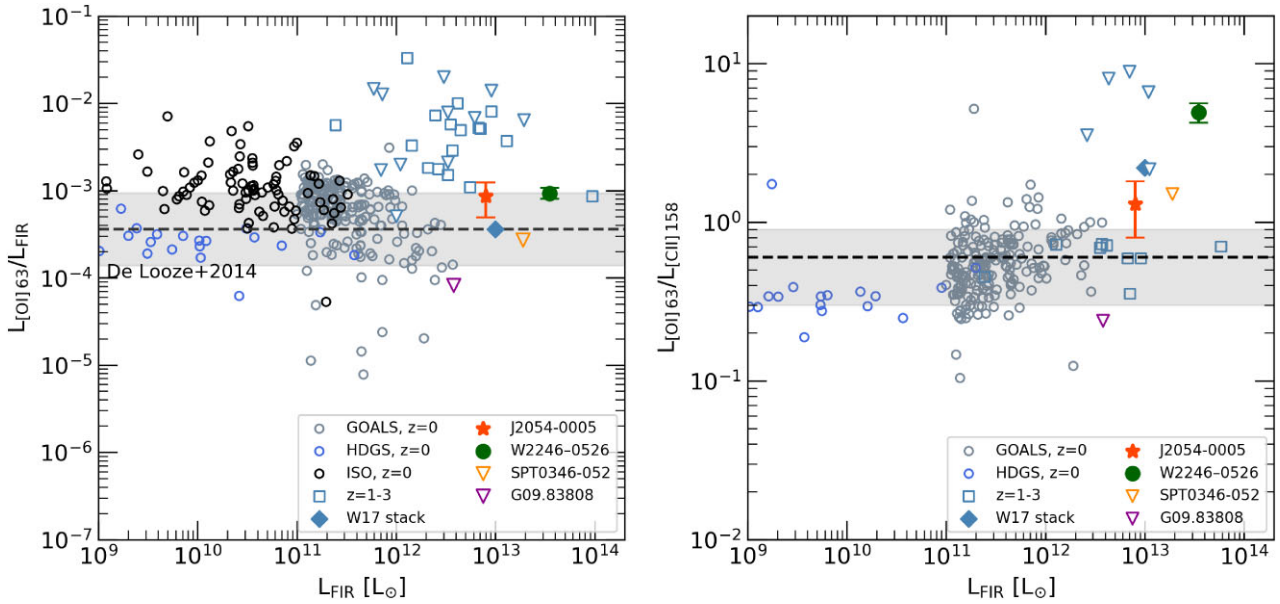


**Fig. 2** (Left) $L_{[O\,I]63\,\mu m}$-to-$L_{FIR}$ ratio plotted against $L_{FIR}$, where the luminosities are corrected for magnification, if any. The red star indicates the quasar J2054−0005 at $z = 6.04$. The other three objects at $z > 4$ are also shown: the detection of [O I] 63 μm in a hyper-luminous AGN W2246−0526 at $z = 4.601$ (Fernández Aranda et al. 2024; green circle), and the non-detections of SMGs G09.83808 at at $z = 6.027$ (Rybak et al. 2023; purple inverted triangle) and SPT 0346–52 at $z = 5.656$ (Litke et al. 2022; orange inverted triangle). The plot includes nearby U/LIRGs from the GOALS survey (Diaz-Santos et al. 2017; small gray circles), blue compact dwarf galaxies from the Herschel Dwarf Galaxy survey (Cormier et al. 2015; small blue circles), and other local galaxies observed by ISO (compiled in Coppin et al. 2012; small black circles). A typical range of $L_{[O\,I]63\,\mu m}/L_{FIR}$ in De Looze et al. (2014) is shown by the horizontal dashed line with a shaded region. Also included are detections and non-detections of [O I] 63 μm at $z \sim 1$–3 (Coppin et al. 2012; Brisbin et al. 2015; Zhang et al. 2018; Wagg et al. 2020; blue squares, non-detections indicated by inverted triangles) and the detection of [O I] 63 μm in a stacked spectrum of four lensed SMGs (Wardlow et al. 2017; blue diamond). The upper limits correspond to 3$\sigma$. (Right) $L_{[O\,I]63\,\mu m}$-to-$L_{[C\,II]158\,\mu m}$ ratio plotted against $L_{FIR}$. The symbols are the same as in the left panel. The median and standard deviation of the local samples are shown as a horizontal black line with a shaded region.

horizontal line with a shaded region indicates the relation between $L_{[O\,I]63\,\mu m}/L_{FIR}$ and $L_{FIR}$, where we convert SFR into $L_{FIR}$ under the assumption of the Salpeter initial mass function (Salpeter 1955; Kennicutt & Evans 2012).

The data also include the individual detections and non-detections of [O I] 63 μm at $z \sim 1$–3 (Coppin et al. 2012; Brisbin et al. 2015; Wardlow et al. 2017; Zhang et al. 2018; Wagg et al. 2020; cyan squares), where the 3$\sigma$ upper limits are shown with inverted triangles. The detection of [O I] 63 μm in a stacked spectrum of five lensed SMGs at $z \sim 1$–3 is also shown (Wardlow et al. 2017; cyan diamond).

We also include the data points of $z > 4$ ALMA observations, where the inverted triangle indicate the 3$\sigma$ upper limits: detection in J2054−0005 (this study; red star), a $z = 4.601$ hyper-luminous AGN W2246−0526 (Fernández Aranda et al. 2024; green circle), non-detection of two submillimeter galaxies (SMGs), G09.83808 at $z = 6.027$ (Rybak et al. 2023; purple inverted triangle) and SPT 0346–52 at $z = 5.656$ (Litke et al. 2022; orange inverted triangle). In this plot, we have corrected for the lensing magnification factors, if any.

The left panel of figure 2 shows that the data points of two [O I] detections at $z > 4$ (J2054−0005 and W2246−0526) are well within the range of the local relation in De Looze et al. (2014), but show lower $L_{[O\,I]63\,\mu m}/L_{FIR}$ than those in the individual detections at $z = 1$–3.

As discussed in Wardlow et al. (2017), the initial campaign of [O I] 63 μm observations in high-$z$ SMGs in Sturm et al. (2010) and Coppin et al. (2012) has indicated that $L_{[O\,I]63\,\mu m}/L_{FIR}$ may be high in the high-$z$ SMG population (cyan squares). On the other hand, the luminosity ratio in the stacked data of high-$z$ SMGs in Wardlow et al. (2017) (cyan diamond) is consistent with the value obtained in the local Universe. Interestingly, the three SMGs in Coppin et al. (2012)[5] and one SMG in Sturm et al. (2010)[6] have AGN activity, which Wardlow et al. (2017) have given as a possible explanation for the enhanced luminosity ratio. However, the situation is complicated as the sample of six SMGs at $z = 1$–2 in Brisbin et al. (2015) uniformly shows high $L_{[O\,I]63\,\mu m}/L_{FIR}$ regardless of the presence of AGN activity, where three of the six objects have AGN activity (cyan squares). Based on the fact that $L_{[O\,I]63\,\mu m}/L_{FIR}$ of the four objects at $z > 4$ is consistent with that in the local Universe, we conclude that high-$z$ SMGs do not necessarily have high $L_{[O\,I]63\,\mu m}/L_{FIR}$.

### 3.3.2 $L_{FIR}$ vs. $L_{[O\,I]63\,\mu m}/L_{[C\,II]158\,\mu m}$

The right panel of figure 2 shows a comparison of $L_{[O\,I]63\,\mu m}/L_{[C\,II]158\,\mu m}$ with the literature values. The symbols are the same as those in the left panel, where the data points of $z = 1$–3 are plotted if the line ratio is available. The median and standard deviation of $L_{[O\,I]63\,\mu m}/L_{[C\,II]158\,\mu m}$ in the local samples are 0.6 and 0.3, respectively (horizontal black line and gray shaded region). The line ratios in the $z = 1$–3 sample range from 0.5 to 2.0. The line ratios in the $z > 4$ objects are $1.3 \pm 0.5$, $4.91 \pm 0.72$, 0.22 (3$\sigma$), and 1.5 (3$\sigma$) for J2054−0005, W2246−0526, G09.83808, and SPT 0346–52, respectively.

[5] The object IDs are LESS66, 88, and 102.
[6] The object ID is MIPS J1248.

$L_{[O\,I]63\,\mu m}/L_{[C\,II]158\,\mu m}$ in J2054−0005 is consistent with the typical value obtained in the local Universe within the uncertainty. On the other hand, W2246−0562 shows the second highest line ratio among the $z = 0$–6 samples.

## 4 Discussion

### 4.1 AGN contribution to [O I] 63 μm in J2054−0005

Previous studies have shown that $L_{[O\,I]63\,\mu m}/L_{[C\,II]158\,\mu m}$ is enhanced in the presence of AGN activity. Based on the observations of 52 objects in the Herschel SHINING survey, Herrera-Camus et al. (2018) have found that only objects with AGN activity reach $L_{[O\,I]63\,\mu m}/L_{[C\,II]158\,\mu m} \gtrsim 1.6$ in the local Universe (see also Fukuchi et al. 2022).

This is consistent with a theoretical study of Abel et al. (2009) that predicts that $L_{[O\,I]63\,\mu m}/L_{[C\,II]158\,\mu m}$ becomes higher in the presence of AGN activity. The calculations of Abel et al. (2009) are based on CLOUDY (Ferland et al. 2013), include both star-formation and AGN activity, and adopt a one-dimensional spherical geometry. The authors have found that $L_{[O\,I]63\,\mu m}/L_{[C\,II]158\,\mu m} \gtrsim 2$ can be achieved only in the presence of AGN activity (see their figure 6). According to Abel et al. (2009), the higher line ratio is due to the fact that X-rays emitted by the AGN activity can penetrate deep into the cloud and heat the gas through photodissociation and photoionization. Similarly, Meijerink, Spaans, and Israel (2007) have presented theoretical predictions for the $L_{[O\,I]63\,\mu m}/L_{[C\,II]158\,\mu m}$ ratio based on models accounting for both star-formation and AGN activity. The result is consistent with Abel et al. (2009) in the sense that the line ratio becomes higher in the presence of AGN activity. However, Meijerink, Spaans, and Israel (2007) have also shown that the line ratio can reach as high as $\sim 40$ with PDR models alone (i.e., without AGN acitivity) if the gas column density of PDR is sufficiently high (see their figure 2). Altogether, both the observational and theoretical studies show that $L_{[O\,I]63\,\mu m}/L_{[C\,II]158\,\mu m}$ is enhanced in the presence of AGN activity, although the exact value of the ratio is model dependent.

In J2054−0005, the observed line ratio of $L_{[O\,I]63\,\mu m}/L_{[C\,II]158\,\mu m} = 1.3 \pm 0.5$ is close to the criterion presented in Abel et al. (2009) and Herrera-Camus et al. (2018) within uncertainties, which does not allow us to strongly conclude whether the AGN activity affects the [O I] 63 μm line emission.

To further check if the AGN activity in J2054−0005 affects [O I] 63 μm, we refer to the results of Decarli et al. (2022) who have concluded that PDRs rather than X-ray dominated regions (XDRs) better reproduce the observed lines of [C II] 158 μm, [C I](2–1), and CO in a sample of $z \sim 6$ luminous quasars including J2054−0005. Briefly, the authors have constructed PDR and XDR models with a wide variety of parameter space in the hydrogen density ($n_H$), incident radiation field, incident X-ray flux, and the total hydrogen column density ($N_{HI}$) based on CLOUDY. The authors have found that the line ratio of $L_{[C\,II]158\,\mu m}/L_{[C\,I](2-1)} > 10$ is achieved in PDRs, while it is <10 in XDRs at the column density of $N_{HI} \gtrsim 10^{22}$ cm$^{-2}$.[7] The observed line ratio of $L_{[C\,II]158\,\mu m}/L_{[C\,I](2-1)} > 30$ indicates that the XDR does not strongly affect the emission lines in J2054−0005 (Decarli et al. 2022). In conclusion, we do not find evidence in J2054−0005 that the emission lines are strongly powered due to the AGN activity.

### 4.2 PDR modeling

Under the assumption that the [O I] 63 μm and [C II] 158 μm lines are emitted not from XDRs but from PDRs in J2054−0005 (subsection 4.1), we examine the PDR properties of J2054−0005 based on comparisons of the observed line luminosities of [O I] 63 μm, [C II] 158 μm, and dust continuum emission (i.e., $L_{FIR}$) to model predictions. These luminosities are commonly used to examine PDR properties (e.g., Hollenbach & Tielens 1999; Malhotra et al. 2001). The $L_{[O\,I]63\,\mu m}/L_{[C\,II]158\,\mu m}$ ratio is sensitive to $n_H$ because the line ratio strongly depends on density beyond the critical density of [C II] 158 μm, $n_{H,crit.} \sim 3 \times 10^3$ cm$^{-3}$, and [O I] 63 μm becomes an important coolant in the PDR at $G/G_0 \gtrsim 100$ (Wolfire et al. 2022). The ratio of $(L_{[O\,I]63\,\mu m} + L_{[C\,II]158\,\mu m})/L_{FIR}$ traces the heating efficiency (Wolfire et al. 2022).

#### 4.2.1 Model descriptions

We employ PDR Toolbox (PDRT; Pound & Wolfire 2008, 2023). The models have two codes, the Wolfire–Kaufman code and the KOSMA-tau code (Röllig et al. 2013; Pound & Wolfire 2023). Following recent observational studies of high-$z$ quasars (e.g., Shao et al. 2019; Yang et al. 2019), we use the latest version of the Wolfire–Kaufman code, which is referred to as the "wk2020" model in Pound and Wolfire (2023). The model assumptions are summarized in table 1 in Pound and Wolfire (2023). Briefly, the model assumes a plane-parallel geometry with UV radiation field, cosmic rays, and soft X-rays incident on one side. The model also assumes abundances of e.g., carbon, oxygen, and polycyclic aromatic hydrocarbons (PAHs). The "wk2020" models have two sets of metallicity, $Z/Z_\odot = 0.5$ and 1.0. In this study, we adopt the case of $Z/Z_\odot = 1.0$.[8]

The two main input parameters are the radiation field strength in terms of Habing fields ($G_0 = 1.6 \times 10^{-3}$ erg cm$^{-2}$ s$^{-1}$) and a constant hydrogen nucleus density, $n_H$. With these two parameters, the model calculates local chemical equilibrium to determine local density, solves local energy balance to estimate temperature and pressure, and performs radiative transfer through a PDR layer to output line intensities from one side. Thus, if more than two intensity ratios are available, one can constrain $n_H$ and the FUV radiation field based on comparisons of the models with observed line intensities. Note that PDRT assumes that [C II] 158 μm is purely emitted from the PDR. In this study, we further assume that [C II], [O I], and dust continuum emission are co-spatial, but discuss this limitation in sub-subsection 4.2.3.

#### 4.2.2 Corrections to input luminosities

Before comparing the models to the line luminosity ratios in J2054−0005, we apply the following three corrections to the data. First, although we assume that the [O I] 63 μm and [C II] 158 μm lines are emitted from PDRs (subsection 4.1), it is possible that the dust continuum emission is partly powered

[7] This is a result of X-rays penetrating more deeply into the clouds than UV photons, thus heating the cloud cores to enhance [C I](2–1) (Decarli et al. 2022; see also Izumi et al. 2020 for the use of [C II]/[C I] to examine the presence of AGN).

[8] Although the metallicity is not obtained for J2054−0005 in the literature due to the lack of lines necessary to estimate it, the choice of the value is motivated by the metallicity estimates in two similarly FIR-luminous quasars: Li et al. (2020b) and Novak et al. (2019) have obtained $Z/Z_\odot = 1.5$–2.1 and 0.7–2.0 for J2310+1855 at $z = 6.0$ and J1342+0928 at $z = 7.54$, respectively.

by the AGN activity in J2054−0005. Based on the results of multi-wavelength SED fitting with CIGALE in Salak et al. (2024), we find that the AGN activity contributes ≈78% of the FIR luminosity on the galactic scale in J2054−0005.[9] We thus adopt the far-infrared luminosity from star-formation activity, $L_{\rm FIR}({\rm PDR}) = 0.22 L_{\rm FIR} = (1.5 \pm 0.1) \times 10^{12}\,L_\odot$.

Secondly, although the PDRT models assume that [C II] 158 μm is purely emitted from PDRs, [C II] originates from both the H II regions and PDR in reality (e.g., Oberst et al. 2006; Herrera-Camus et al. 2016). We assume that 17% of [C II] 158 μm is emitted from the H II regions based on a result for a similarly FIR-luminous quasar, J2310+1855 at $z = 6.0$[10] (Li et al. 2020a). The [C II] 158 μm luminosity emitted from PDR, $L_{[\rm C\,II]158\,\mu m}({\rm PDR})$, is estimated to be $0.83 L_{[\rm C\,II]158\,\mu m} = (2.8 \pm 0.4) \times 10^9 L_\odot$.

Finally, in a more realistic geometry of spherical clouds, the optically thin emission (FIR continuum and [C II] 158 μm) would be detected from both the front and back sides of the cloud, whereas the optically thick emission ([O I] 63 μm) would be detected only from the front side[11] (Kaufman et al. 1999; Röllig et al. 2007; Yang et al. 2019). Following previous studies (e.g., Wardlow et al. 2017; Yang et al. 2019; Hashimoto et al. 2023), we multiply the observed luminosity of [O I] 63 μm by a factor of two, $L_{[\rm O\,I]63\,\mu m,\,corr.} = 2 L_{[\rm O\,I]63\,\mu m} = (9.1 \pm 3.0) \times 10^9\,L_\odot$.

### 4.2.3 Results of PDR modeling

Figure 3 shows the results of PDR modeling in J2054−0005. The darker red and blue shaded regions indicate the parameter space allowed by $L_{[\rm O\,I]63\,\mu m}/L_{[\rm C\,II]158\,\mu m}$ and $(L_{[\rm C\,II]158\,\mu m} + L_{[\rm O\,I]63\,\mu m})/L_{\rm FIR}$, respectively. We obtain a fiducial result, $\log(n_{\rm H}/{\rm cm}^{-3}) = 3.7 \pm 0.3$ and $\log(G/G_0) = 3.0 \pm 0.1$, as indicated by a thick black circle. Here, we only consider the solution with $\log(G/G_0) \gtrsim 1$ as physically plausible following the discussion in Brisbin et al. (2015).

Because the correction to $L_{\rm FIR}$ in sub-subsection 4.2.2 is not usually applied even in the presence of AGN activity (e.g., Brisbin et al. 2015), as a comparison, we also perform PDR modeling with the same models without applying the correction to $L_{\rm FIR}$ (purple shaded region). As indicated by a black dotted circle, the result, $\log(n_{\rm H}/{\rm cm}^{-3}) = 3.4 \pm 0.4$ and $\log(G/G_0) = 3.7 \pm 0.3$, is shifted toward a higher FUV radiation field compared to the fiducial case. Given the possible uncertainty in the correction of $L_{\rm FIR}$, the FUV radiation field of $\log(G/G_0) \sim 3.7$ can be regarded as the upper limit.

We further discuss two considerations in the PDR modeling. First, the [O I] 63 μm line may be self-absorbed as described above. Given the limited quality of our data, it is difficult to determine conclusively if the line in J2054−0005 is indeed self-absorbed. However, by closely comparing the [O I] 63 μm line profile to that of [C II] 158 μm as shown in figure 4, we

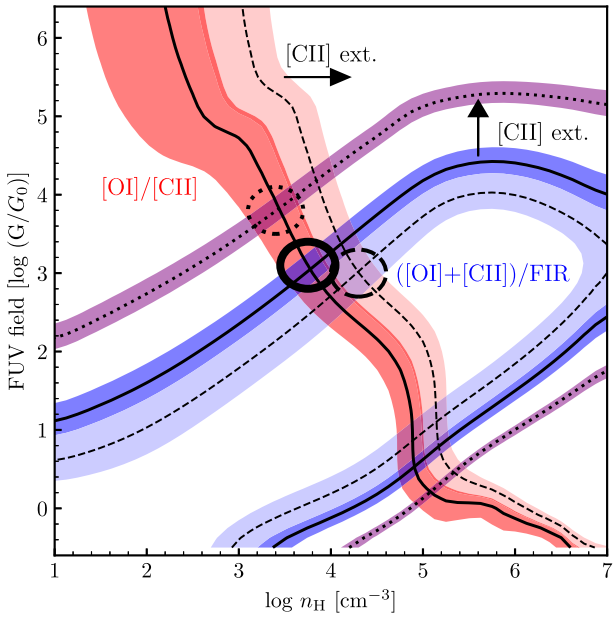


**Fig. 3** FUV radiation field, $G$, and the hydrogen gas density, $n_{\rm H}$, that reproduce the luminosity ratios of J2054−0005. We use the "wk2020" models of PDRToolbox (Pound & Wolfire 2023). The darker red and blue shaded regions indicate the parameter space allowed by $L_{[\rm O\,I]63\,\mu m}/L_{[\rm C\,II]158\,\mu m}$ and $(L_{[\rm C\,II]158\,\mu m} + L_{[\rm O\,I]63\,\mu m})/L_{\rm FIR}$, respectively, where the black solid lines correspond to the median luminosity ratios. In this fiducial case, we have applied the following corrections to the luminosities (see sub-subsection 4.2.2 for details): removal of the AGN contribution to $L_{\rm FIR}$, removal of the H II region contribution to $L_{[\rm C\,II]158\,\mu m}$, and multiplication of $L_{[\rm O\,I]63\,\mu m}$ by a factor of two. The fiducial result, $\log(n_{\rm H}/{\rm cm}^{-3}) = 3.7 \pm 0.3$ and $\log(G/G_0) = 3.0 \pm 0.1$, is shown by a thick black circle. The lighter red and blue shaded regions indicate the parameter space if [O I] 63 μm is self-absorbed by a factor of two, i.e., $L_{[\rm O\,I]63\,\mu m}$ multiplied by an additional factor of two (see sub-subsection 4.2.3). The black dashed lines correspond to the median luminosity ratios. The result, $\log(n_{\rm H}/{\rm cm}^{-3}) = 4.3 \pm 0.3$ and $\log(G/G_0) = 3.0 \pm 0.4$, is shown by a black dashed circle. As a reference, the purple shaded region and the dotted line indicate the parameter space if no correction is applied to $L_{\rm FIR}$. The result, $\log(n_{\rm H}/{\rm cm}^{-3}) = 3.4 \pm 0.4$ and $\log(G/G_0) = 3.7 \pm 0.3$, is shown by a black dotted circle. Two black arrows indicate the direction of correction to account for the different spatial size of [C II] 158 μm and dust continuum emission.

can make a tentative assessment. In this figure, we show the spectrum at a finer resolution of 30 km s$^{-1}$. Examining the two lines in figure 4, if we assume that the [O I] 63 μm line is not self-absorbed, then its line peak is ∼ 50 km s$^{-1}$ blueward of the [C II] peak, with a line width about half as narrow as the [C II] line. While this scenario is not impossible, especially if the [C II] line is more spatially extended, it may also be hinting that some of the [O I] line has been self-absorbed. To assess how much, a two-component Gaussian fit is made to the [O I] data. For the fit we assume that the [O I] emission should arise in the same regions as the [C II] so we force one component to the same line center and line width as the [C II] line, letting only its amplitude vary. The second component is left completely unconstrained. The result of the non-linear least-squares fit via *SciPy*'s ODR module is shown in figure 4. The best-fitting model includes an absorption component at ∼100 km s$^{-1}$ with an FWHM of ∼ 80 km s$^{-1}$. Integrating the emission component we get an estimated line flux of $2.9 \pm 0.7$ Jy km s$^{-1}$, about 50% higher than if we assume that the line is not self-absorbed. Given the low signal-to-noise ratio of the spectrum, this exact value should be treated cautiously,

[9] In Salak et al. (2024), the fractional AGN contribution to the IR luminosity is computed based on work by Fritz, Franceschini, and Hatziminaoglou (2006) that assumes three components through a radiative transfer: primary source located in the torus, the scattered emission by dust, and the thermal dust emission.

[10] The contribution from the H II regions can be estimated with the luminosity ratio of [C II]-to-[N II] 205 μm. However, [N II] 205 μm is not observed in J2054−0005.

[11] [C II] 158 μm becomes optically thick at the column density of $N({\rm C}^+) = 5 \times 10^{17}$ cm$^{-2}$ at a velocity width of 4 km s$^{-1}$ (Russell et al. 1980). On the other hand, the optical depth of [O I] 63 μm becomes unity at a column density of $N({\rm O}^0) = 2 \times 10^{17}$ cm$^{-2}$ at a velocity width of 1 km s$^{-1}$ (Wolfire et al. 2022). Because $O^0$ is present up to higher optical depth clouds than $C^+$, [O I] 63 μm becomes optically thick faster than [C II] 158 μm (Malhotra et al. 2001).

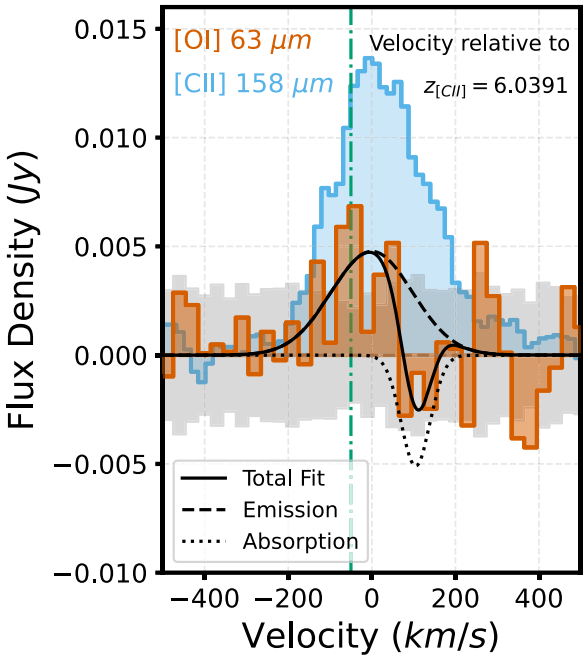


**Fig. 4** [O I] 63 μm (orange) with error (gray) plotted over the [C II] line (blue) from Wang et al. (2013). The [O I] 63 μm line, if it is not self-absorbed, appears narrow and has a line center (green dash–dotted) that is ∼50 km s$^{-1}$ blueward of the [C II] line, suggesting different spatial extents of the two emission lines in J2054−0005. If we assume that both lines arise in the same regions, consistent with our PDR modeling, then the [O I] spectrum is well described via self-absorption with a two-component Gaussian model (solid black) including emission (dashed black) and absorption (dotted black) components.

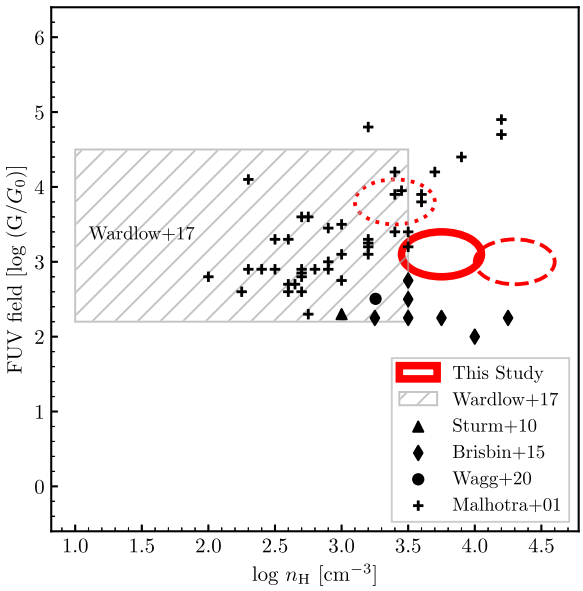


**Fig. 5** Comparisons of the FUV radiation field, $G$, and the hydrogen gas density, $n_H$, obtained for J2054−0005 with the literature values. In J2054−0005, three results are shown with red circles (see figure 3). The black crosses show the results of nearby star-forming galaxies (Malhotra et al. 2001). The black triangle and diamonds indicate the results of a lensed $z \sim 1$ SMG (Sturm et al. 2010) and unlensed SMGs at $z \sim 1$–2 (Brisbin et al. 2015). The black circle shows a $z \sim 1$ BzK galaxy (Wagg et al. 2020). The region with a hatch corresponds to the result of a stacked spectrum of $z \sim 1$–3 SMGs in Wardlow et al. (2017). J2054−0005 has PDR properties broadly consistent with those in the literature.

but it does suggest that the [O I] 63 μm line in J2054−0005 may indeed be self-absorbed. To account for this possibility, we also perform PDR modeling by multiplying the [O I] 63 μm line luminosity by an additional factor of two[12] (lighter red and blue shaded regions in figure 3). As indicated by a black dashed circle, the result, $\log(n_H/\mathrm{cm}^{-3}) = 4.3 \pm 0.3$ and $\log(G/G_0) = 3.0 \pm 0.4$, is slightly shifted toward a higher gas density.

Secondly, the [C II] 158 μm, [O I] 63 μm, and dust continuum emission are not necessarily co-spatial. Deep ALMA imaging has revealed extended, diffuse [C II] "halos" around high-$z$ star-forming galaxies (e.g., Gullberg et al. 2018; Fujimoto et al. 2019, 2020; Rybak et al. 2019, 2020; Ikeda et al. 2024). Recently, based on the high angular resolution data of [C II] 158 μm in the ALMA-CRISTAL survey, Ikeda et al. (2024) have found that the spatial extent of [C II] can be explained by PDRs, while the contribution from diffuse neutral medium (atomic gas) and the effects of mergers may further expand the [C II] line distributions. In the case of J2054−0005, high-resolution ALMA imaging indicates that the [C II] emission is a factor of ≈2 more extended than dust (Venemans et al. 2020). In figure 3, we show an arrow indicating the direction of the correction due to the extended [C II], where we divide the [C II] luminosity by a factor of two. A detailed discussion is hampered by the fact that the spatial extent of [O I] is not known. Future higher-resolution observation of [O I] 63 μm is crucial for more sophisticated PDR modeling.

[12] As discussed in Wolfire, Vallini, and Chevance (2022), the correction to [O I] 63 μm in the case of self-absorption is typically 2–4. This is also in agreement, within the uncertainties, with the unabsorbed flux estimated via our Gaussian fitting.

#### 4.2.4 Comparisons of our PDR modeling to the literature

In figure 5, we compare the results of J2054−0005 with the literature values. Black crosses and a black triangle show the results in nearby star-forming galaxies (Malhotra et al. 2001) and a lensed $z \sim 1$ SMG (Sturm et al. 2010), respectively. These results are obtained based on the models of Kaufman et al. (1999) with the [O I] 63 μm, [C II] 158 μm, and IR luminosities. Black diamonds indicate the results in non-lensed SMGs at $z \sim 1$–2 (Brisbin et al. 2015). The authors have used the PDR models of Pound and Wolfire (2008) with the [O I] 63 μm, [C II] 158 μm, and IR luminosities. A black circle shows the result of Wagg et al. (2020) in a BzK galaxy at $z \sim 1$. The PDR modeling is based on the models of Wolfire, Vallini, and Chevance (2022) with the [O I] 63 μm, CO(2–1), and IR luminosities. Finally, we also plot the result of Wardlow et al. (2017) who have performed PDR modeling for a stacked spectrum of $z \sim 1$–3 SMGs. The authors have used the models of Pound and Wolfire (2008) and the [O I] 63 μm, [C II] 158 μm, [Si III] 34 μm, and IR luminosities.

As can be seen in figure 5, the samples of nearby star-forming galaxies and $z = 1$–3 SMGs with individual detections of [O I] 63 μm exhibit a broad range of gas density, ranging from $\log(n_H/\mathrm{cm}^{-3}) \sim 2$ to $> 4$. The PDR properties of J2054−0005 are broadly consistent with these galaxies; however, we note that J2054−0005 falls within the region that overlaps with the high-$\log(n_H)$ objects among the star-forming galaxies. This is consistent with a picture that the gas is centrally concentrated in the quasar host galaxy, leading to the stimulation of both intense nuclear star

formation and central supermassive black hole accretion (e.g., Hopkins et al. 2008).

## 5 Summary

We have presented [O I] 63 μm data of a luminous quasar, J2054−0005 at $z = 6.04$ obtained with ALMA Band 9. The [O I] 63 μm line is detected at the peak significance level of 5.0 at the expected position and frequency (figure 1). To date, this is the highest-$z$ detection of [O I] 63 μm, and only the second case of [O I] 63 μm detection at $z > 4$ after a hyper-luminous AGN, W2246−0526 (Fernández Aranda et al. 2024). Our findings are summarized as follows.

- In J2054−0005, the [O I] 63 μm line luminosity is $(4.5 \pm 1.5) \times 10^9 L_\odot$, corresponding to $L_{[\mathrm{O\,I}]63\,\mu\mathrm{m}}/L_{\mathrm{FIR}} = (6.7 \pm 2.2) \times 10^{-4}$. We have compiled the data points of objects with [O I] 63 μm observations at $z = 0$–4, and compared them with J2054−0005. In contrast to the previous [O I] 63 μm detections in individual SMGs at $z = 1$–3 that show enhanced $L_{[\mathrm{O\,I}]63\,\mu\mathrm{m}}/L_{\mathrm{FIR}}$ against the local value, we have found that the values in J2054−0005 and W2246−0526 at $z = 4$–6 are consistent with those in the local Universe (left panel of figure 2). In J2054−0005, [O I] 63 μm is as bright as [C II] 158 μm, resulting in $L_{[\mathrm{O\,I}]63\,\mu\mathrm{m}}/L_{[\mathrm{C\,II}]158\,\mu\mathrm{m}} = 1.3 \pm 0.5$ (right panel of figure 2).
- Analyzing the [O I] 63 μm spectrum and fitting a two-component Gaussian model suggests that the [O I] 63 μm line may be self-absorbed. Deeper observations of the line to significantly detect the absorption feature are necessary to conclusively determine the degree of self-absorption (figure 4).
- We have performed PDR modeling with PDRT (Pound & Wolfire 2023) based on the luminosity ratios of $L_{[\mathrm{O\,I}]63\,\mu\mathrm{m}}/L_{[\mathrm{C\,II}]158\,\mu\mathrm{m}}$ and $(L_{[\mathrm{O\,I}]63\,\mu\mathrm{m}} + L_{[\mathrm{C\,II}]158\,\mu\mathrm{m}})/L_{\mathrm{FIR}}$. We have carefully removed the possible contribution of AGN activity to $L_{\mathrm{FIR}}$ and the H II contribution to $L_{[\mathrm{C\,II}]158\,\mu\mathrm{m}}$. We have obtained the gas density of $\log(n_{\mathrm{H}}/\mathrm{cm}^{-3}) = 3.7 \pm 0.3$ and FUV radiation field of $\log(G/G_0) = 3.0 \pm 0.1$, although the results can slightly change if we consider the self-absorption effect on [O I] 63 μm. The PDR properties are in broad agreement with those obtained in nearby star-forming galaxies and other $z = 1$–3 SMGs with individual [O I] 63 μm detections (figures 3 and 5). We note that J2054−0005 falls within the region that overlaps with the high-$\log(n_{\mathrm{H}})$ objects among the star-forming galaxies.

## Acknowledgments

The authors thank the referee for comments and suggestions that helped us improve the manuscript. We also acknowledge Ken Ohsuga, Ryota Ikeda, Atsushi Yasuda, Saho Kawahara, Ryota Ura, Tatsuya Matsumura, and Yu Nagai for useful discussion. TH was supported by the Leading Initiative for Excellent Young Researchers, MEXT, Japan (HJH02007) and by JSPS KAKENHI grant Nos. 20K22358 and 22H01258. MR was supported by the NWO Veni project "*Under the lens*" (VI.Veni.202.225). TM was supported by a University Research Support Grant from the National Astronomical Observatory of Japan (NAOJ). DD acknowledges support from the National Science Center (NCN) grant SONATA (UMO-2020/39/D/ST9/00720). KM acknowledges support from the Japan Society for the Promotion of Science (JSPS) through KAKENHI grant No. 20K14516. YT was supported by KAKENHI grant Nos. 22H04939 and 23K20035. TI was supported by KAKENHI No. 23K03462. YN acknowledges funding from JSPS KAKENHI Grant Number 23KJ0728. This paper makes use of the following ALMA data: ADS/JAO.ALMA#2016.1.01063.S. ALMA is a partnership of ESO (representing its member states), NSF (USA) and NINS (Japan), together with NRC (Canada), MOST and ASIAA (Taiwan), and KASI (Republic of Korea), in cooperation with the Republic of Chile. The Joint ALMA Observatory is operated by ESO, AUI/NRAO and NAOJ.

## References

Abel, N. P., Dudley, C., Fischer, J., Satyapal, S., & van Hoof, P. A. M. 2009, ApJ, 701, 1147
Baluteau, J.-P., et al. 1997, A&A, 322, L33
Boquien, M., Burgarella, D., Roehlly, Y., Buat, V., Ciesla, L., Corre, D., Inoue, A. K., & Salas, H. 2019, A&A, 622, A103
Brauher, J. R., Dale, D. A., & Helou, G. 2008, ApJS, 178, 280
Brisbin, D., Ferkinhoff, C., Nikola, T., Parshley, S., Stacey, G. J., Spoon, H., Hailey-Dunsheath, S., & Verma, A. 2015, ApJ, 799, 13
CASA Team 2022, PASP, 134, 114501
Coppin, K. E. K., et al. 2012, MNRAS, 427, 520
Cormier, D., et al. 2015, A&A, 578, A53
De Looze, I., et al. 2014, A&A, 568, A62
Decarli, R., et al. 2018, ApJ, 854, 97
Decarli, R., et al. 2022, A&A, 662, A60
Díaz-Santos, T., et al. 2017, ApJ, 846, 32
Draine, B. T. 2011, Physics of the Interstellar and Intergalactic Medium (Princeton, NJ: Princeton University Press)
Farina, E. P., et al. 2022, ApJ, 941, 106
Farrah, D., et al. 2013, ApJ, 776, 38
Ferland, G. J., et al. 2013, Rev. Mex. Astron. Astrofis., 49, 137
Fernández Aranda, R., et al. 2024, A&A, 682, A166
Fritz, J., Franceschini, A., & Hatziminaoglou, E. 2006, MNRAS, 366, 767
Fujimoto, S., et al. 2019, ApJ, 887, 107
Fujimoto, S., et al. 2020, ApJ, 900, 1
Fukuchi, H., et al. 2022, ApJ, 940, 7
Furniss, I., Jennings, R. E., King, K. J., Lightfoot, J. F., Emery, R. J., Naylor, D. A., & Fitton, B. 1983, MNRAS, 202, 859
Goldsmith, P. F., Langer, W. D., Seo, Y., Pineda, J., Stutzki, J., Guevara, C., Aladro, R., & Justen, M. 2021, ApJ, 916, 6
González-Alfonso, E., et al. 2012, A&A, 541, A4
Gullberg, B., et al. 2018, ApJ, 859, 12
Hashimoto, T., et al. 2023, ApJ, 952, 48
Hashimoto, T., Inoue, A. K., Tamura, Y., Matsuo, H., Mawatari, K., & Yamaguchi, Y. 2019, PASJ, 71, 109
Herrera-Camus, R., et al. 2016, ApJ, 826, 175
Herrera-Camus, R., et al. 2018, ApJ, 861, 94
Hollenbach, D. J., & Tielens, A. G. G. M. 1999, Rev. Modern Phys., 71, 173
Hopkins, P. F., Hernquist, L., Cox, T. J., & Kereš, D. 2008, ApJS, 175, 356
Ikeda, R., et al. 2024, arXiv:2408.03374
Inayoshi, K., Visbal, E., & Haiman, Z. 2020, ARA&A, 58, 27
Izumi, T., et al. 2019, PASJ, 71, 111
Izumi, T., et al. 2020, ApJ, 898, 75
Jiang, L., et al. 2008, AJ, 135, 1057
Kaasinen, M., et al. 2023, A&A, 671, A29
Kaufman, M. J., Wolfire, M. G., & Hollenbach, D. J. 2006, ApJ, 644, 283

Kaufman, M. J., Wolfire, M. G., Hollenbach, D. J., & Luhman, M. L. 1999, ApJ, 527, 795
Kennicutt, R. C., & Evans, N. J. 2012, ARA&A, 50, 531
Komatsu, E., et al. 2011, ApJS, 192, 18
Kormendy, J., & Ho, L. C. 2013, ARA&A, 51, 511
Kraemer, K. E., Jackson, J. M., & Lane, A. P. 1998, ApJ, 503, 785
Li, J., et al. 2020a, ApJ, 900, 131
Li, Z., Li, Z., Smith, M. W. L., & Gao, Y. 2020b, ApJ, 905, 138
Litke, K. C., et al. 2022, ApJ, 928, 179
Madden, S. C., et al. 2013, PASP, 125, 600
Malhotra, S., et al. 2001, ApJ, 561, 766
Meijerink, R., Spaans, M., & Israel, F. P. 2007, A&A, 461, 793
Melnick, G., Gull, G. E., & Harwit, M. 1979, ApJ, 227, L29
Narayanan, D., & Krumholz, M. R. 2017, MNRAS, 467, 50
Novak, M., et al. 2019, ApJ, 881, 63
Oberst, T. E., et al. 2006, ApJ, 652, L125
Pensabene, A., et al. 2024, A&A, 684, A119
Poglitsch, A., Herrmann, F., Genzel, R., Madden, S. C., Nikola, T., Timmermann, R., Geis, N., & Stacey, G. J. 1996, ApJ, 462, L43
Pound, M. W., & Wolfire, M. G. 2008, ASP Conf. Ser., 394, 654
Pound, M. W., & Wolfire, M. G. 2023, AJ, 165, 25
Röllig, M., et al. 2007, A&A, 467, 187
Röllig, M., Szczerba, R., Ossenkopf, V., & Glück, C. 2013, A&A, 549, A85
Rosenberg, M. J. F., et al. 2015, ApJ, 801, 72
Russell, R. W., Melnick, G., Gull, G. E., & Harwit, M. 1980, ApJ, 240, L99
Rybak, M., et al. 2019, ApJ, 876, 112
Rybak, M., et al. 2023, Res. Notes American Astron. Soc., 7, 188
Rybak, M., Zavala, J. A., Hodge, J. A., Casey, C. M., & van der Werf, P. 2020, ApJ, 889, L11
Salak, D., et al. 2024, ApJ, 962, 1
Salpeter, E. E. 1955, ApJ, 121, 161
Shao, Y., et al. 2019, ApJ, 876, 99
Solomon, P. M., Downes, D., & Radford, S. J. E. 1992, ApJ, 387, L55
Sturm, E., et al. 2010, A&A, 518, L36
Tripodi, R., et al. 2024, A&A, 689, A220
Uzgil, B. D., Bradford, C. M., Hailey-Dunsheath, S., Maloney, P. R., & Aguirre, J. E. 2016, ApJ, 832, 209
Valiante, R., Agarwal, B., Habouzit, M., & Pezzulli, E. 2017, Publ. Astron. Soc. Australia, 34, e031
Venemans, B. P., et al. 2018, ApJ, 866, 159
Venemans, B. P., et al. 2020, ApJ, 904, 130
Wagg, J., et al. 2020, MNRAS, 499, 1788
Wang, R., et al. 2013, ApJ, 773, 44
Wardlow, J. L., et al. 2017, ApJ, 837, 12
Wolfire, M. G., Vallini, L., & Chevance, M. 2022, ARA&A, 60, 247
Yang, J., et al. 2019, ApJ, 880, 153
Zhang, Z.-Y., et al. 2018, MNRAS, 481, 59

Received: 2024 August 20; Accepted: 2024 November 26